Journal of Thermal Analysis and Calorimetry (2019) 138:2219–2231
https://doi.org/10.1007/s10973-019-08323-4

Synthesis and thermal, optical and magnetic properties of new Mn^{2+}-doped and Eu^{3+}-co-doped scheelites

M. Karolewicz[1] · H. Fuks[2] · E. Tomaszewicz[1]

Received: 30 October 2018 / Accepted: 27 April 2019 / Published online: 28 May 2019

Abstract

A series of Mn^{2+}-doped and Eu^{3+}-co-doped calcium molybdato-tungstates, i.e., $Ca_{1-3x-y}Mn_y\square_xEu_{2x}(MoO_4)_{1-3x}(WO_4)_{3x}$ ($0 < x \leq 0.2222$ when $y = 0.0200$ and $0 < y \leq 0.0667$ when $x = 0.1667$, $\square$ represents vacancy) materials were successfully synthesized via high-temperature annealing. XRD results confirmed the formation of single, tetragonal scheelite-type phases (space group $I4_1/a$). A change in both lattice constants (a and c), lattice parameter ratio c/a and progressive deformation of MoO_4/WO_4 tetrahedra with increasing Eu^{3+} as well as Mn^{2+} contents were observed. The melting point of doped materials is lower than the melting point of pure matrix, i.e., $CaMoO_4$. New materials exhibit strong absorption in the UV range. They are insulators with the optical direct band gap (E_g) higher than 3.50 eV. The E_g values nonlinearly change with increasing dopants concentrations. EPR measurements allowed to establish the nature of magnetic interactions among Mn^{2+} ions. Additionally, EPR spectra were sensitive on both parameters: Mn^{2+} and Eu^{3+} concentration.

Keywords Scheelites · Sintering · Thermal stability · Optical properties · Magnetic properties

Introduction

Metal molybdates and tungstates were proved to be excellent host lattice of luminescent materials due to their high thermal stability and chemical tolerance. These compounds show many different types of structures, i.e., scheelite ($I4_1/a$, No. 88), pseudo-scheelite (*Pnma*, No. 62), wolframite ($P2/c$, No. 13), zircon ($I4_1/amd$, No. 141) and fergusonite (C2/c, No. 15) [1–7]. Most divalent metal molybdates and tungstates take scheelite-type or scheelite-related structure. Scheelite-type $A(Mo,W)O_4$ compounds possess eight symmetry elements, a body-centered unit cell and four molecules per one unit cell [1–3, 6, 7]. Each A-site divalent ion is surrounded by eight oxygen anions and forms AO_8 dodecahedra [1–3, 6, 7]. Each Mo^{6+} or W^{6+} ion is coordinated to four oxygen ions forming $(Mo, W)O_4$ tetrahedron [1–3, 6, 7].

Materials doped with trivalent rare-earth (RE) ions have been studied for many applications, such as lasers, solid state lightings, display panels and optical amplifiers [8]. Among of trivalent RE ions, Eu^{3+} ion is characterized by the lowest excited level $^5D_0$ of $4f^6$ configuration and displayed mainly very sharp red light emission centered at 615 nm ascribed to the $^5D_0 \rightarrow {}^7F_2$ transition [9]. Divalent manganese ion plays an important role in some inorganic phosphors. It can produce a broad emission due to the transition from $^4T_1$ to $^6A_1$ level. The emission color strongly depends on a crystal field strength as well as coordination number of Mn^{2+}, and it varies from green (tetrahedral coordination of manganese ions) to red (octahedrally coordinated Mn^{2+}) [10–14]. Thus, simultaneously doping the host material with Eu^{3+} and Mn^{2+} ions allows to energy transfer from Mn^{2+} to Eu^{3+} ions and improve the luminescent efficiency of doped samples [15, 16].

In our earlier papers, we have focused on three scheelite-type matrices, i.e., $CdMoO_4$, $PbMoO_4$ and $PbWO_4$. Our studies have shown the existence of new scheelite-type solid solutions described by the following chemical

✉ E. Tomaszewicz
tomela@zut.edu.pl

[1] Department of Inorganic and Analytical Chemistry, Faculty of Chemical Technology and Engineering, West Pomeranian University of Technology, Szczecin, Al. Piastów 42, 71-065 Szczecin, Poland

[2] Institute of Physics, West Pomeranian University of Technology, Szczecin, Al. Piastów 48, 70-311 Szczecin, Poland

formulas: $(Cd,Pb)_{1-3x}\square_xRE_{2x}MoO_4$ and $(Cd,Pb)_{1-3x}\square_xRE_{2x}(MoO_4)_{1-3x}(WO_4)_{3x}$, where RE = Pr–Yb [17–26]. The substitution of divalent Cd^{2+} or Pb^{2+} ions by trivalent rare-earth ones is connected with a charge-compensating defect. Charge balance is achieved by the formation of A-site vacancies, which is denoted by us as □, i.e., $3\ Cd^{2+}(Pb^{2+}) \rightarrow 2\ RE^{3+} + \square$. Presence of these vacancies is seen in the dependence of wavenumber and integral intensity of some electronic absorption, IR and Raman bands on increasing concentration of the point defects in the RE^{3+}-doped materials. The presence of vacancies results also in significant deformation of the crystal lattice, particularly around RE^{3+} ions, and which results in the emission of broadbands associated with *f–f* transitions in RE^{3+} ions [19–21]. The RE^{3+}-doped molybdates or molybdato-tungstates are promising laser materials, phosphors and good microwave dielectric microcrystalline ceramics for band-pass filters, resonators and antenna switches (mobile and satellite communication) [19–22].

In this work, microcrystalline samples of new $Ca_{1-3x-y}Mn_y\square_xEu_{2x}(MoO_4)_{1-3x}(WO_4)_{3x}$ solid solution with different Mn^{2+} (y = 0.0066; 0.0200; 0.0333; 0.0667) as well as Eu^{3+} (x = 0.0005; 0.0025; 0.0050; 0.0098; 0.0283; 0.0455; 0.0839; 0.1430; 0.1667; 0.1970; 0.2059; 0.2222) contents were successfully obtained by a high-temperature sintering. Their structure, thermal stability and optical properties were examined. Electron paramagnetic resonance spectroscopy (EPR) was used to determine the types of magnetic interactions and the local symmetry of Mn^{2+} ions.

Experimental

Synthesis of $Ca_{1-3x-y}Mn_y\square_xEu_{2x}(MoO_4)_{1-3x}(WO_4)_{3x}$

New microcrystalline Mn^{2+}-doped and Eu^{3+}-co-doped calcium molybdato-tungstates with the following formula of $Ca_{1-3x-y}Mn_y\square_xEu_{2x}(MoO_4)_{1-3x}(WO_4)_{3x}$ were obtained by the two-step synthesis, in which both the steps consist of high-temperature sintering which is very often used in a preparation of many molybdates and tungstates [27–32]. The following reactants were used in the first step of synthesis: $CaCO_3$, MnO, MoO_3, Eu_2O_3 and WO_3 (all raw materials of high-purity grade min. 99.95%, Alfa Aesar or Fluka, and without thermal pre-treatment). Calcium molybdate ($CaMoO_4$), manganese molybdate ($MnMoO_4$) as well as europium tungstate $Eu_2(WO_4)_3$ were obtained according to the procedure used by us in previous studies [26, 32]. In the next step of synthesis, we prepared 15 ternary mixtures containing $MnMoO_4$, $Eu_2(WO_4)_3$ and $CaMoO_4$. The concentrations of manganese molybdate and europium tungstate in each initial $MnMoO_4/Eu_2(WO_4)_3/CaMoO_4$ mixture are shown in Table 1. The initial mixtures, not compacted to pellets, were heated in air, in ceramic crucibles, in several 12-h annealing stages, and at temperatures in the range of 1173–1473 K. After each heating period, obtained materials were cooled down to ambient temperature, weighed, ground in an agate mortar, followed by examination for their composition by XRD method. The mass change control of doped samples showed a slight mass loss observed for each material that did not exceed the value of 0.26%. This observation suggests that a synthesis of new materials runs practically without their mass change.

Methods

Powder X-ray diffraction patterns of new doped materials were collected within the 2θ range of 10°–100° and under ambient conditions by using an EMPYREAN II diffractometer (PANalytical) and CuKα1,2 radiation (the scanning step 0.013°). High Score Plus 4.0 software was used to analyze registered XRD patterns. Lattice parameters were calculated using the procedure described and used in our previous works [17–26, 32]. Quantachrome Instruments Ultrapycnometer (model Ultrapyc 1200 e) was used to measure the density of each sample. As the pycnometric gas, nitrogen (purity 99.99%) was used. DTA-TG studies of manganese molybdate and europium tungstate were carried out on a TA Instruments thermoanalyzer (model SDT 2960) at the heating rate of 10 K min^{-1}, and in the temperature range from 293 to 1473 K (the air flow 110 mL min^{-1}). Melting point of some Mn^{2+}-doped and Eu^{3+}-co-doped ceramic materials was determined by using a pyrometric method. Selected samples, previously compressed into pellets, were heated in a resistance furnace, and their image was simultaneously recorded by a camera. Melting point of a sample was determined at the time when its image was not seen in a camera. IR spectra were recorded within the spectral range of 1500–200 cm^{-1} on a Specord M-80 spectrometer (Carl Zeiss Jena) using pellets with potassium bromide. UV–Vis reflectance spectra were recorded within the range of 200–1000 nm using JASCO-V670 spectrophotometer containing an integrating sphere. EPR spectra of Mn^{2+}-doped and Eu^{3+}-co-doped samples were determined by an X-band Bruker ELEXSYS E 500 CW spectrometer operating at 9.5 GHz with 100 kHz magnetic field modulation. Temperature dependence of the EPR spectra of doped materials within the 78–300 K temperature range was recorded using Oxford Instruments ESP liquid nitrogen and helium cryostat.

Table 1 Lattice constants, experimental and calculated X-ray density, and determined optical direct band gap, E_g of $Ca_{1-3x-y}Mn_y\square_xEu_{2x}(MoO_4)_{1-3x}(WO_4)_{3x}$

$Eu_2(WO_4)_3$ content [mol %]	$MnMoO_4$ content [mol %]	Formula of solid solution		Lattice constants/Å		Density/ $g\cdot cm^{-3}$		*Eg*/ eV	References
				a	*c*	d_{exp}	d_{rtg}		
$Ca_{1-3x-y}Mn_y\square_xEu_{2x}(MoO_4)_{1-3x}(WO_4)_{3x}$ $y = 0.0200$									
0	0	$x = 0$	$CaMoO_4$	5.22961(12)	11.4410(4)	4.24(2)	4.24	3.81	[35]
0.05	3.00	$x = 0.0005$	$Ca_{0.9785}Mn_{0.0200}\square_{0.0005}Eu_{0.0010}(MoO_4)_{0.9985}(WO_4)_{0.0015}$	5.22498(10)	11.4245(3)	4.27(1)	4.26	3.78	This work
0.25	3.00	$x = 0.0025$	$Ca_{0.9725}Mn_{0.0200}\square_{0.0025}Eu_{0.0050}(MoO_4)_{0.9925}(WO_4)_{0.0075}$	5.22535(15)	11.4252(5)	4.28(2)	4.29	3.75	This work
0.50	3.00	$x = 0.0050$	$Ca_{0.9650}Mn_{0.0200}\square_{0.0050}Eu_{0.0100}(MoO_4)_{0.9850}(WO_4)_{0.0150}$	5.22585(9)	11.4284(4)	4.29(3)	4.31	3.74	This work
1.00	3.00	$x = 0.0098$	$Ca_{0.9506}Mn_{0.0200}\square_{0.0098}Eu_{0.0196}(MoO_4)_{0.9706}(WO_4)_{0.0294}$	5.22628(14)	11.4266(2)	4.33(2)	4.36	3.73	This work
3.00	3.00	$x = 0.0283$	$Ca_{0.8951}Mn_{0.0200}\square_{0.0283}Eu_{0.0566}(MoO_4)_{0.9151}(WO_4)_{0.0849}$	5.22894(8)	11.4228(2)	4.60(1)	4.53	3.68	This work
5.00	3.00	$x = 0.0455$	$Ca_{0.8435}Mn_{0.0200}\square_{0.0455}Eu_{0.0910}(MoO_4)_{0.8635}(WO_4)_{0.1365}$	5.23098(12)	11.4232(3)	4.74(1)	4.69	3.63	This work
10.00	3.00	$x = 0.0839$	$Ca_{0.7283}Mn_{0.0200}\square_{0.0839}Eu_{0.1678}(MoO_4)_{0.7483}(WO_4)_{0.2517}$	5.23649(7)	11.4229(2)	5.10(2)	5.04	3.65	This work
20.00	3.00	$x = 0.1430$	$Ca_{0.5510}Mn_{0.0200}\square_{0.1430}Eu_{0.2860}(MoO_4)_{0.5710}(WO_4)_{0.4290}$	5.24204(10)	11.4319(4)	5.63(1)	5.59	3.54	This work
25.00	3.00	$x = 0.1667$	$Ca_{0.4799}Mn_{0.0200}\square_{0.1667}Eu_{0.3334}(MoO_4)_{0.4999}(WO_4)_{0.5001}$	5.24352(12)	11.4424(5)	5.79(1)	5.80	3.59	This work
32.50	3.00	$x = 0.1970$	$Ca_{0.3890}Mn_{0.0200}\square_{0.1970}Eu_{0.3940}(MoO_4)_{0.4090}(WO_4)_{0.5910}$	5.24383(8)	11.4635(3)	6.13(2)	6.08	3.46	This work
35.00	3.00	$x = 0.2059$	$Ca_{0.3623}Mn_{0.0200}\square_{0.2059}Eu_{0.4118}(MoO_4)_{0.3823}(WO_4)_{0.6177}$	5.24455(15)	11.4612(6)	6.15(2)	6.16	3.54	This work
40.00	3.00	$x = 0.2222$	$Ca_{0.3134}Mn_{0.0200}\square_{0.2222}Eu_{0.4444}(MoO_4)_{0.3334}(WO_4)_{0.6666}$	5.24556(11)	11.4718(4)	6.28(3)	6.31	3.54	This work
$Ca_{1-3x-y}Mn_y\square_xEu_{2x}(MoO_4)_{1-3x}(WO_4)_{3x}$ $x = 0.1667$									
25.00	1.00	$y = 0.0066$	$Ca_{0.4933}Mn_{0.0066}\square_{0.1667}Eu_{0.3334}(MoO_4)_{0.4999}(WO_4)_{0.5001}$	5.24422(16)	11.4477(5)	5.76(1)	5.79	3.60	This work
25.00	5.00	$y = 0.0333$	$Ca_{0.4666}Mn_{0.0333}\square_{0.1667}Eu_{0.3334}(MoO_4)_{0.4999}(WO_4)_{0.5001}$	5.23814(9)	11.4272(3)	5.79(1)	5.83	3.56	This work
25.00	10.00	$y = 0.0667$	$Ca_{0.4332}Mn_{0.0667}\square_{0.1667}Eu_{0.3334}(MoO_4)_{0.4999}(WO_4)_{0.5001}$	5.23240(10)	11.4020(4)	5.83(1)	5.86	3.68	This work

The formula of each solid solution was calculated on phase composition of initial $MnMoO_4$//$Eu_2(WO_4)_3$/$CaMoO_4$ mixtures and using the proposed model of solid solution

Results and discussion

XRD analysis

The powder diffraction patterns of pure $CaMoO_4$ and $Ca_{1-3x-y}Mn_y\square_xEu_{2x}(MoO_4)_{1-3x}(WO_4)_{3x}$ ceramics with different contents of europium(III) and manganese ions, i.e., when x = 0.0005; 0.0025; 0.0050; 0.0098; 0.0283; 0.0455; 0.0839; 0.1430; 0.1667; 0.1970; 0.2059; and 0.2222 for constant Mn^{2+} content (y = 0.0200) as well as when y = 0.0066; 0.0200; 0.0333; and 0.0667 for constant Eu^{3+} concentration (x = 0.1667) are shown in Fig. 1a, b. XRD analysis shows the powder diffraction patterns of Mn^{2+}-doped and Eu^{3+}-co-doped calcium molybdatotungstates consisted of diffraction lines which can be attributed to scheelite-type framework. No impurity phases, i.e., initial reactants, oxides (Eu_2O_3, MnO, CaO, MoO_3 and WO_3), and other europium tungstates or molybdates were observed with increasing Eu^{3+} concentration only up to x = 0.2222 (40.00 mol% of $Eu_2(WO_4)_3$ in initial $MnMoO_4/Eu_2(WO_4)_3/CaMoO_4$ mixtures when y = constant). No additional phases we have also observed on the powder diffraction patterns of doped materials when Mn^{2+} content was only up to y = 0.0667 (10.00 mol% of $MnMoO_4$ when x = 0.1667). The observed peaks attributed to scheelite-type structure shifted toward lower 2θ angle with increasing Eu^{3+} concentration (Fig. 1a) or toward higher 2θ angle with increasing Mn^{2+} content (Fig. 1b). All observed diffraction lines were successfully indexed to the pure tetragonal scheelite-type structure with space group $I4_1/a$ (No. 88, $CaMoO_4$—JCPDs No. 04-013-6763). This fact confirmed the formation of new solid solution of $MnMoO_4$ and $Eu_2(WO_4)_3$ in $CaMoO_4$ matrix. The diffraction patterns of samples comprising initially above 40.00 mol% $Eu_2(WO_4)_3$ in $MnMoO_4/Eu_2(WO_4)_3/CaMoO_4$ mixtures (not presented in the paper) revealed simultaneously peaks which can be ascribed to the saturated solid solution, i.e., $Ca_{0.3134}Mn_{0.0200}\square_{0.2222}Eu_{0.4444}(MoO_4)_{0.3334}(WO_4)_{0.6666}$ (x = 0.2222) as well as the diffraction lines characteristic of $Eu_2(WO_4)_3$. It means that the solubility limit of europium tungstate in structure of $CaMoO_4$ when the concentration of $MnMoO_4$ equals 3.00 mol% is not higher than 40.00 mol%. On the other hand, the diffraction patterns of samples with an initial content of manganese molybdate above 10.00 mol% showed diffraction lines attributed to $Ca_{0.4332}Mn_{0.0667}\square_{0.1667}Eu_{0.3334}(MoO_4)_{0.4999}(WO_4)_{0.5001}$ (y = 0.0667) as well as the diffraction lines characteristic of $MnMoO_4$. It means that the solubility limit of manganese

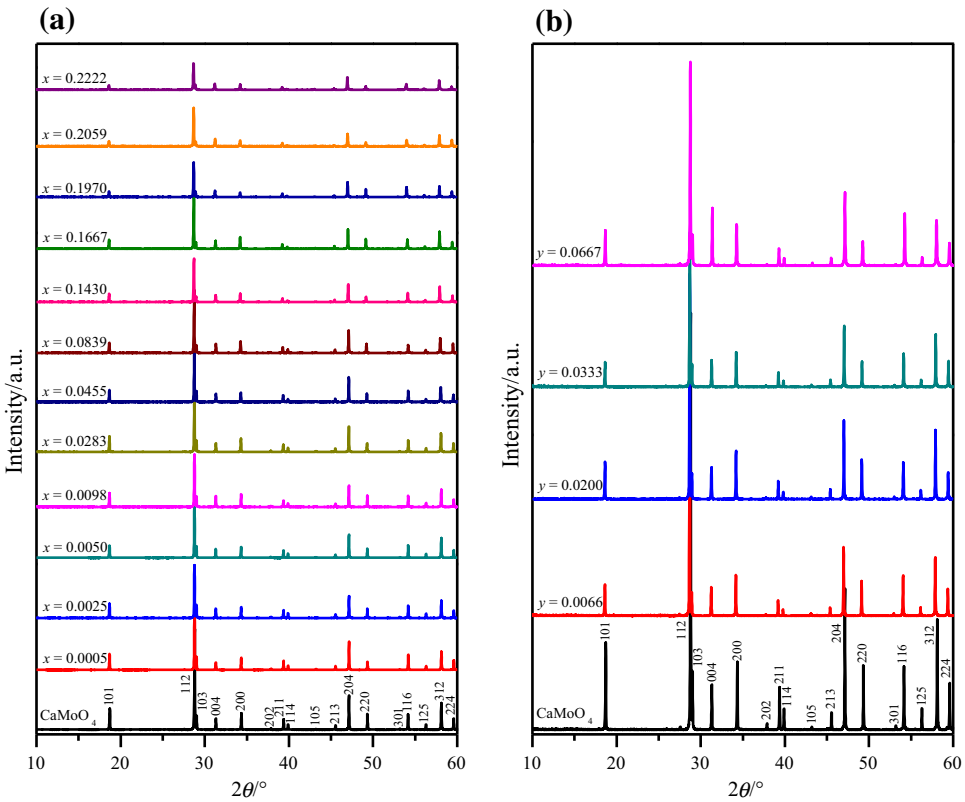

Fig. 1 XRD patterns of $CaMoO_4$ and $Ca_{1-3x-y}Mn_y\square_xEu_{2x}(MoO_4)_{1-3x}(WO_4)_{3x}$ ceramics in the 2θ range of 10°–60°. Powder XRD patterns of $0 < x \leq 0.2222$ and y = 0.0200 (**a**) and powder XRD patterns of $0 < y \leq 0.0667$ and x = 0.1667 (**b**)

molybdate in structure of $CaMoO_4$ when the initial concentration of $Eu_2(WO_4)_3$ equals 25.00 mol% is not higher than 10.00 mol%.

The lattice constants calculated on the basic of XRD data for $CaMoO_4$ as well as for Mn^{2+}-doped and Eu^{3+}-co-doped ceramics are presented in Table 1. Both unit cell parameters (a and c) of doped materials gradually increased with increasing Eu^{3+} concentration when Mn^{2+} content in samples was constant ($y = 0.0200$). This is not a typical situation because bigger Ca^{2+} ions (112 pm for CN = 8) in the matrix were substituted by much smaller Eu^{3+} ones (106.6 pm for CN = 8) [33]. We have already observed this phenomenon in other RE^{3+}-doped and vacancied materials, i.e., $Cd_{1-3x}\square_xDy_{2x}MoO_4$ [22]. The lattice parameters of all doped samples decreased gradually with increasing Mn^{2+} concentration for the materials with constant Eu^{3+} content (Table 1). It is a consequence of the substitution of big Ca^{2+} ions by much smaller Mn^{2+} ones (96 pm for CN = 8). In all scheelite-type molybdates and tungstates, Mo^{6+} and W^{6+} ions are tetrahedrally coordinated by oxygen ones and their ionic radii are 41 and 42 pm, respectively [33]. Thus, the substitution of Mo^{6+} by W^{6+} observed in $Ca_{1-3x-y}Mn_y\square_xEu_{2x}(MoO_4)_{1-3x}(WO_4)_{3x}$ materials did not cause any visible changes in both lattice constants. Only a parameter as well as the volume of tetragonal cell (V) calculated for doped ceramics (when Eu^{3+} concentration was increasing and Mn^{2+} content was constant) obeys the Vegard's law, i.e., they are nearly linear functions of x parameter (Fig. 2). The c parameter changes clearly nonlinearly with increasing Eu^{3+} content in the samples (Fig. 3, Table 1). In contrast, the lattice parameters (both a and c) as well as the volume of cell calculated for doped samples (when Mn^{2+} content was increasing and Eu^{3+} concentration was constant) obey the Vegard's law when $0 < y \leq 0.0667$ (Figs. 4, 5). We also calculated the lattice parameter ratio c/a for two series of Mn^{2+}-doped and Eu^{3+}-co-doped ceramics (Figs. 3, 5). This parameter clearly nonlinearly changes with increasing x (Fig. 3) as well as practically linearly decreases with increasing y (Fig. 5). It means that in whole homogeneity range of $Ca_{1-3x-y}Mn_y\square_xEu_{2x}(MoO_4)_{1-3x}(WO_4)_{3x}$ solid solution we have observed a deformation of tetragonal scheelite-type cell of each doped sample in comparison with the tetragonal cell of pure $CaMoO_4$. The experimental density values determined for each sample under study are

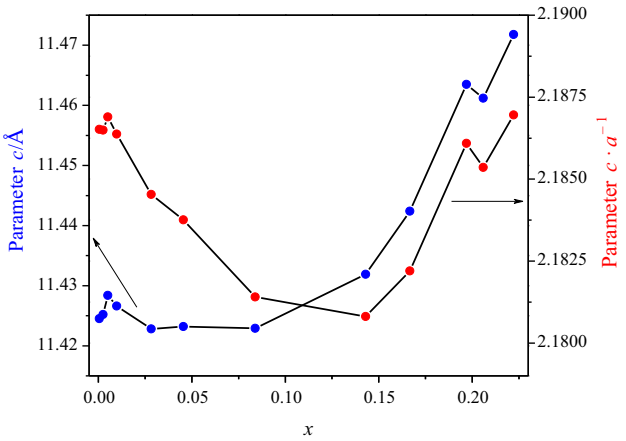

Fig. 3 Dependences of c parameter and $c \cdot a^{-1}$ versus x parameter of $0 < x \leq 0.2222$ and $y = 0.0200$

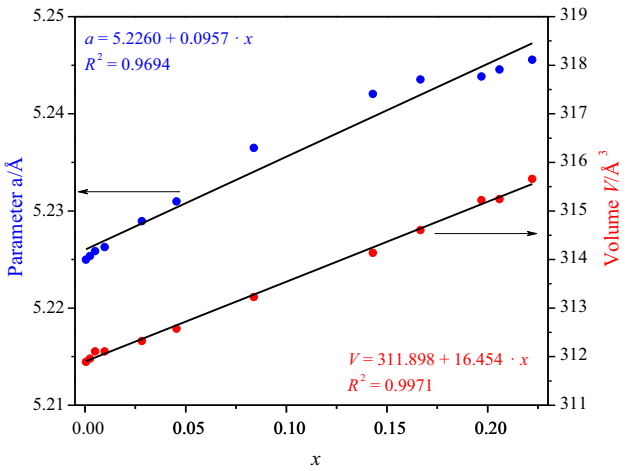

Fig. 2 Linear dependences of a parameter and volume V versus x parameter of $0 < x \leq 0.2222$ and $y = 0.0200$

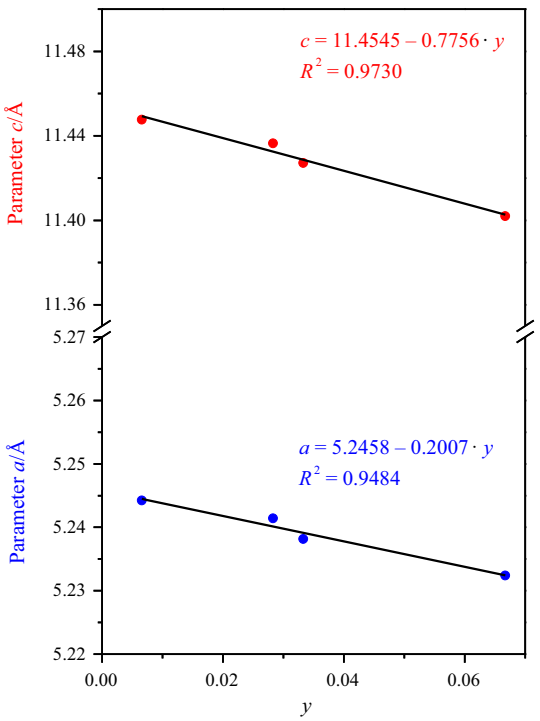

Fig. 4 Linear dependences of both a and c lattice constants versus x parameter of $0 < y \leq 0.0667$ and $x = 0.1667$

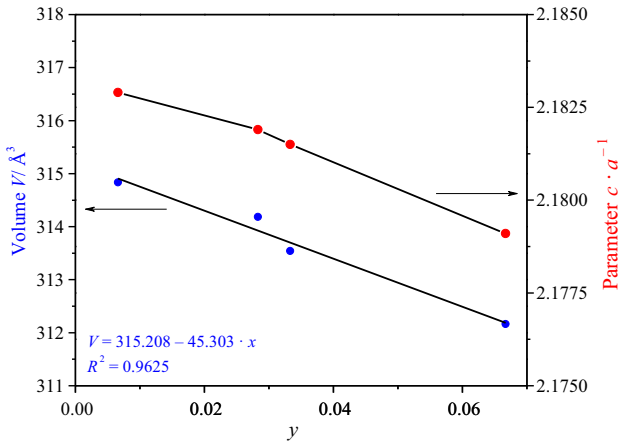

Fig. 5 Linear dependences of volume V and $c \cdot a^{-1}$ versus x parameter of $0 < y \leq 0.0667$ and $x = 0.1667$

given in Table 1. The density of $Ca_{1-3x-y}Mn_y\square_xEu_{2x}(MoO_4)_{1-3x}(WO_4)_{3x}$ samples almost linearly increases with increasing Eu^{3+} as well as Mn^{2+} content (Table 1).

Thermal stability of $Ca_{1-3x-y}Mn_y\square_xEu_{2x}(MoO_4)_{1-3x}(WO_4)_{3x}$ materials

Appropriate thermal studies of new Mn^{2+}-doped and Eu^{3+}-co-doped microceramics have been preceded by DTA experiments for some initial reactants, i.e., $MnMoO_4$ and $Eu_2(WO_4)_3$, due to the fact that information on their thermal properties is not completely, contrary or unknown. Figure 6a shows DTA curve of $MnMoO_4$ recorded during controlled heating up to 1473 K. The single and very sharp endothermic effect with its onset at 1412 K is due to congruent melting of monoclinic manganese molybdate ($a = 4.818(1)$ Å, $b = 5.759(1)$ Å, $c = 4.965(1)$ Å, $\beta = 90.82(1)°$, $Z = 2$, space group $P2/c$ [34]). Only one endothermic peak is observed on DTA curve recorded during controlled heating of $Eu_2(WO_4)_3$ (Fig. 6b). This effect with its onset at 1426 K is connected with congruent melting of monoclinic europium tungstate ($a = 7.676(3)$ Å, $b = 11.463(3)$ Å, $c = 11.396(5)$ Å, $\beta = 109.63(4)°$, $Z = 4$, space group $C2/c$ [35]). In contrary to isostructural $Gd_2(WO_4)_3$, europium tungstate does not show polymorphism [35]. Crystallization process of $Eu_2(WO_4)_3$ from a melt observed during controlled cooling (exothermic effect) is quite significantly shifted toward lower temperatures, and it starts at 1408 K. Pure matrix of $Ca_{1-3x-y}Mn_y\square_xEu_{2x}(MoO_4)_{1-3x}(WO_4)_{3x}$ solid solution, i.e., $CaMoO_4$ melts congruently at 1753 K and this temperature has already been determined in our previous studies by using a pyrometric method [32]. Melting point of some Mn^{2+}-doped and Eu^{3+}-co-doped materials has also been determined by using the same method. These values are lower than the melting point of $CaMoO_4$, and they are as follows: 1653 K ($x = 0.0455$, $y = 0.0200$),

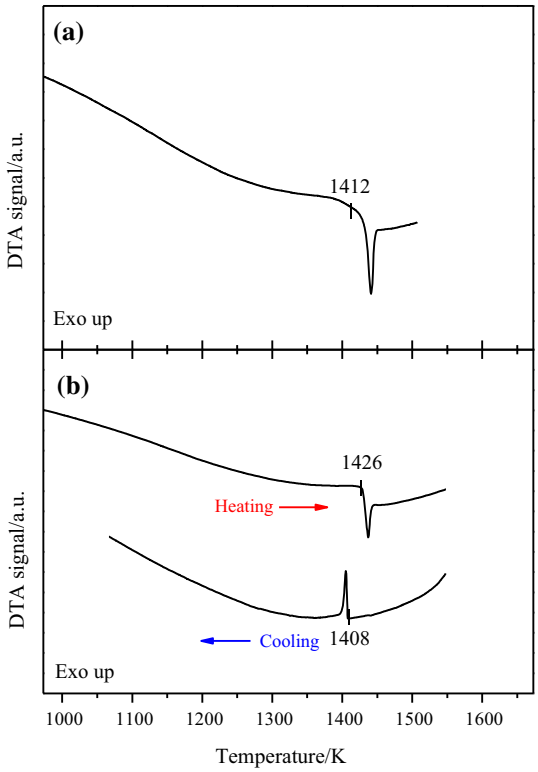

Fig. 6 DTA curves of $MnMoO_4$ (**a**) and $Eu_2(WO_4)_3$ (**b**)

1578 K ($x = 0.1430$, $y = 0.0200$), 1528 K ($x = 0.1970$, $y = 0.0200$), 1503 K ($x = 0.2222$, $y = 0.0200$) and 1518 K ($x = 0.1667$, $y = 0.0667$). Figure 7 shows powder diffraction patterns of some initial Mn^{2+}- and Eu^{3+}-doped materials as well as resulting melts obtained after their pyrometric studies. According to XRD analysis, the patterns of each melt consisted of only diffraction lines which can be attributed to a scheelite-type framework. However, the observed peaks shifted toward lower or higher 2Θ angle in comparison with diffraction lines recorded on the powder XRD patterns of initial Mn^{2+}- and Eu^{3+}-doped materials.

IR spectra

Figures 8 and 9 show the IR spectra of $Ca_{1-3x-y}Mn_y\square_xEu_{2x}(MoO_4)_{1-3x}(WO_4)_{3x}$ microceramics with different contents of Eu^{3+} as well as Mn^{2+} ions, respectively. Molybdates and tungstates with scheelite-type structure are characterized by molecules containing XO_4 (X = Mo or W) tetrahedra showing strong covalent X–O bonds. For scheelite-type materials, the frequencies active in IR are observed within the spectral region of 900–700 cm^{-1} ($\nu_1(A_1)$—symmetric—as well as $\nu_3(F_2)$—asymmetric stretching modes) and 450–250 cm^{-1} ($\nu_2(E_1)$—symmetric—and $\nu_4(F_2)$—asymmetric bending modes) [36–41]. Figures 8 and 9 show IR spectra of pure $CaMoO_4$ and Mn^{2+}-doped and Eu^{3+}-co-doped materials. Strong and narrow

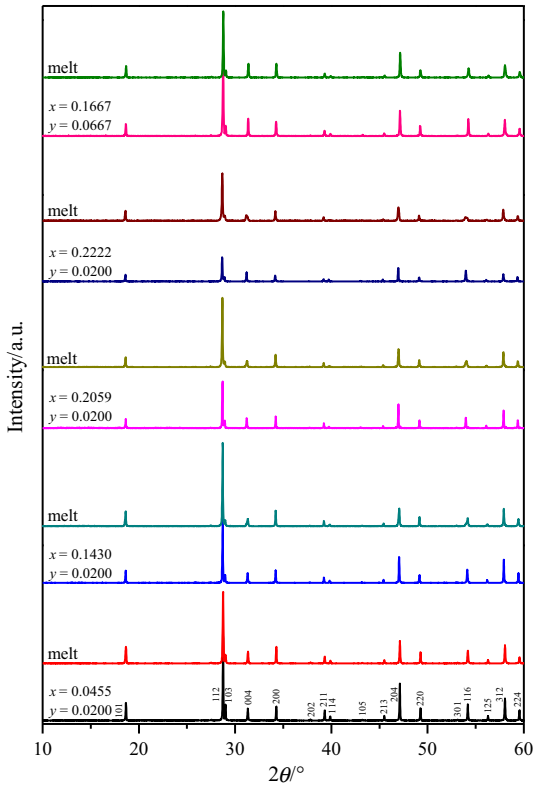

Fig. 7 XRD patterns of $Ca_{1-3x-y}Mn_y\square_xEu_{2x}(MoO_4)_{1-3x}(WO_4)_{3x}$ ceramics in the 2θ range of 10°–60° (x = 0.0455; x = 0.1430; x = 0.2059; x = 0.2222 and y = 0.0200 and x = 0.1667 and y = 0.0667) and their molten forms

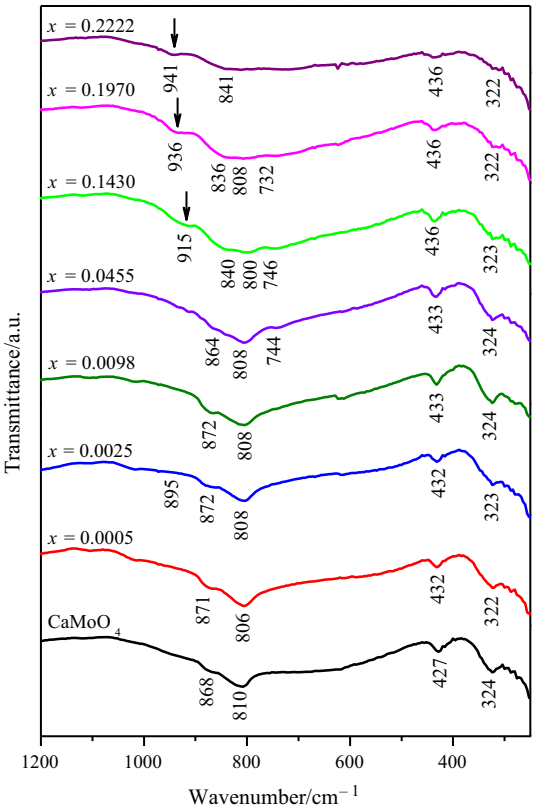

Fig. 8 IR spectra of $CaMoO_4$ and $Ca_{1-3x-y}Mn_y\square_xEu_{2x}(MoO_4)_{1-3x}(WO_4)_{3x}$ (x = 0.0005; x = 0.0025; x = 0.0098; x = 0.0455; x = 0.1430; x = 0.1970; x = 0.2222 and y = 0.0200)

absorption bands observed in the IR spectra of $CaMoO_4$ at 868 and 810 cm^{-1} can be assigned to the stretching modes of Mo–O bonds in MoO_4 tetrahedra [36–41]. The bands with their maximum at 427 and 324 cm^{-1} can be related to the binding modes of Mo–O bonds in MoO_4 tetrahedra [36–41]. The experimental results for calcium molybdate confirm a presence of only regular molybdate tetrahedra occupying sites of a cubic point symmetry T_d characteristic for scheelite-type structure [36–41]. The IR spectra of doped ceramics show differences in an intensity and a width of observed absorption bands compared to those ones registered for pure matrix. They are wide and exhibit very low intensity. Additionally, with increasing content of Eu^{3+} in doped materials, the absorption bands moved toward higher wave numbers (Fig. 8). This phenomenon is clearly visible for bands due to bending vibrations of Mo–O bonds in MoO_4 tetrahedra (Figs. 8, 9). It suggests the presence of tungstate tetrahedra in a crystal lattice of $Ca_{1-3x-y}Mn_y\square_xEu_{2x}(MoO_4)_{1-3x}(WO_4)_{3x}$. For the samples when $x \geq 0.1430$ we can observe additional absorption bands within the region of 940–915 cm^{-1} (Figs. 8, 9). This fact suggests the presence of other types of MoO_4 and WO_4 tetrahedra, i.e., distorted molybdate and tungstate anions. Deformation of the shape of both anions, i.e., changes in X–O and O–X–O bond lengths and/or angles in XO_4 tetrahedra, compared to the shape of regular ones is a result of a presence of vacancies near corners of MoO_4 or WO_4 polyhedra. This deformation of regular tetrahedral shape of molybdate anions had already been observed in vacancied scheelite-type cadmium molybdates doped with RE ions, i.e., $Cd_{0.25}\square_{0.25}RE_{0.50}MoO_4$, where RE = Pr, Nd, Sm–Dy as well as for $Cd_{1-3x}\square_xGd_{2x}MoO_4$ [42, 43].

Optical properties of Mn^{2+}-doped and Eu^{3+}-co-doped ceramics

Optical energy band gap (E_g) of $Ca_{1-3x-y}Mn_y\square_xEu_{2x}(MoO_4)_{1-3x}(WO_4)_{3x}$ ceramics was determined by the method first used by Kubelka and Munk [44] and next applied by many authors [22–25, 32, 45–49]. This method is based on a transformation of diffuse reflectance spectra to estimate band gap energy values. In a case of parabolic band gap structure, an optical energy band gap as well as an absorption coefficient of material (α) can be calculated using the equation proposed by Tauc et al. [50, 51]:

$$ahn = A(hn - E_g)^n, \quad (1)$$

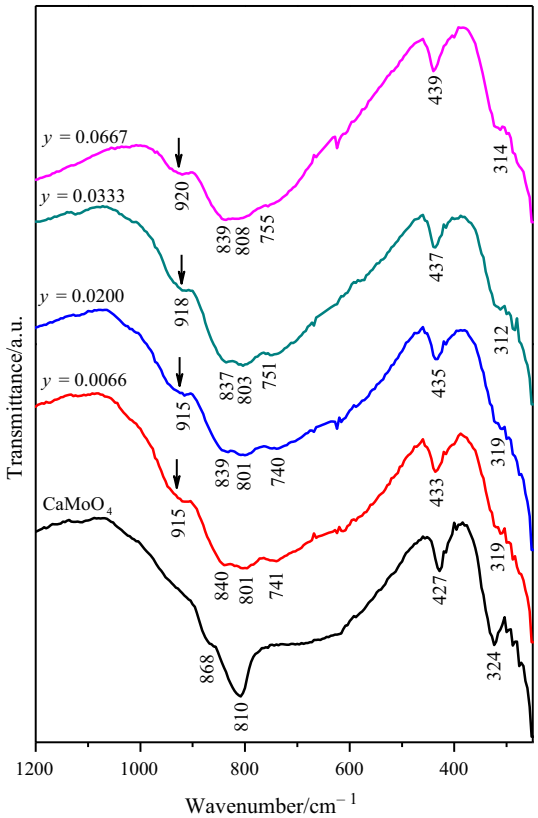

Fig. 9 IR spectra of $CaMoO_4$ and $Ca_{1-3x-y}Mn_y\square_xEu_{2x}(MoO_4)_{1-3x}(WO_4)_{3x}$ of $0 < y \leq 0.0667$ and $x = 0.1667$

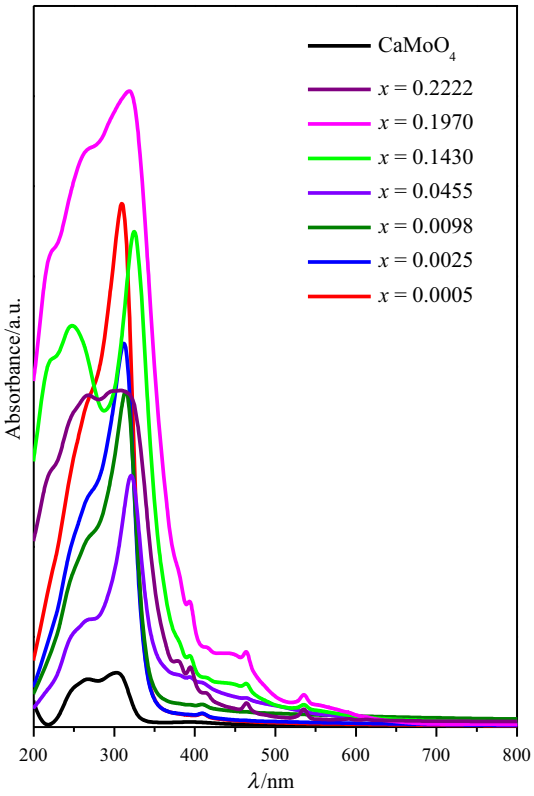

Fig. 10 UV–Vis absorption spectra of $CaMoO_4$ and $Ca_{1-3x-y}Mn_y\square_xEu_{2x}(MoO_4)_{1-3x}(WO_4)_{3x}$ ($x = 0.0005$; $x = 0.0025$; $x = 0.0098$; $x = 0.0455$; $x = 0.1430$; $x = 0.1970$; $x = 0.2222$ and $y = 0.0200$)

where h is the Planck constant, ν is the light frequency, A is the proportionally coefficient characteristic for material under study, and n is the constant determined by an electronic transition type, and it can reach the following values: 1/2, 3/2, 2 and 3 for allowed directly, forbidden directly, allowed indirectly and forbidden indirectly transition, respectively [50, 51]. As it is known from literature information, all alkaline earth metal molybdates and tungstates with the tetragonal scheelite-type structure exhibit an optical absorption spectrum governed by direct absorption transition (n = 1/2). It means that an electron located in a maximum energy state in a valence band reaches a minimum energy state in a conduction band under the same point in the Brillouin zone [52–56]. Thus, the optical band gap of materials can be determined from the plots of $(\alpha h\nu)^2$ as a function of photon energy ($h\nu$) by extrapolating the linear portion of the curve to intersect the $h\nu$ axis at zero absorption [22–25, 32, 45–49, 52–56]. Figures 10 and 11 show UV–Vis absorption spectra of pure $CaMoO_4$ and Mn^{2+}- and Eu^{3+}-doped materials recorded within the spectral range of 200–800 nm. All samples show energy absorption ability in the UV region, and the absorption edge is near to 325 or 350 nm. The plots $(\alpha h\nu)^2$ versus $h\nu$ and the extrapolated direct energy band gap E_g values are shown in Figs. 12 and 13 as well as are given in Table 1, respectively. The E_g values of $Ca_{1-3x-y}Mn_y\square_xEu_{2x}(MoO_4)_{1-3x}(WO_4)_{3x}$ ceramics are lower than the adequate value for pure matrix, and they nonlinearly change with increasing Eu^{3+} content when Mn^{2+} concentration was constant. We have also observed the same nonlinear dependence of E_g with increasing Mn^{2+} content when Eu^{3+} concentration was constant. The lowest value of E_g (3.46 eV) was found for the sample with $x = 0.1970$ and $y = 0.0200$ (Table 1).

EPR results

A group of doped materials with formula of $Ca_{1-3x-y}Mn_y\square_xEu_{2x}(MoO_4)_{1-3x}(WO_4)_{3x}$ with different combination of x and y parameters were studied using the EPR technique. Resonance spectra detected at temperature range of 78–300 K revealed an existence of multiline signal centered near 340 mT magnetic field (Figs. 14, 15). Observed resonance signal could be ascribed to the Mn^{2+} magnetic ions. Manganese metal is characterized by electronic spin value S = 5/2, giving usually a single asymmetric line in EPR experiment. But mentioned ion possesses nuclear spin value I = 5/2, resulting with characteristic splitting of the resonance signal to form six narrow lines.

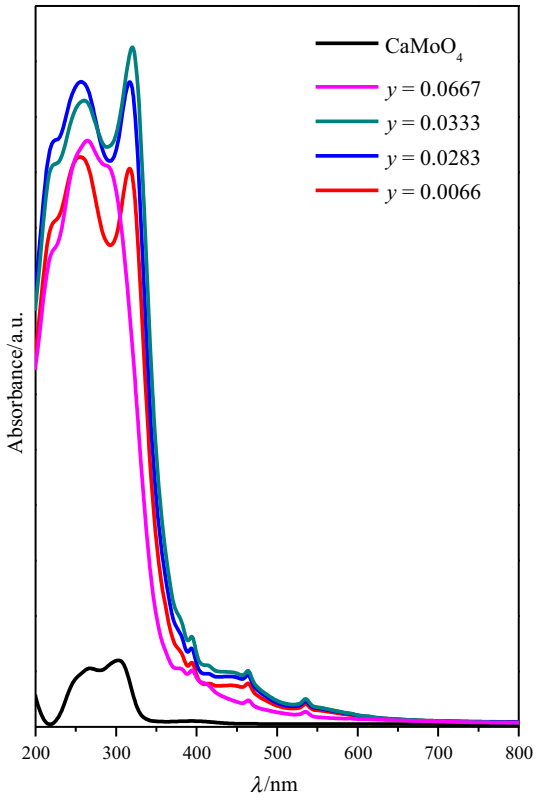

Fig. 11 UV–Vis absorption spectra of $CaMoO_4$ and $Ca_{1-3x-y}Mn_y\square_xEu_{2x}(MoO_4)_{1-3x}(WO_4)_{3x}$ of $0 < y \leq 0.0667$ and $x = 0.1667$

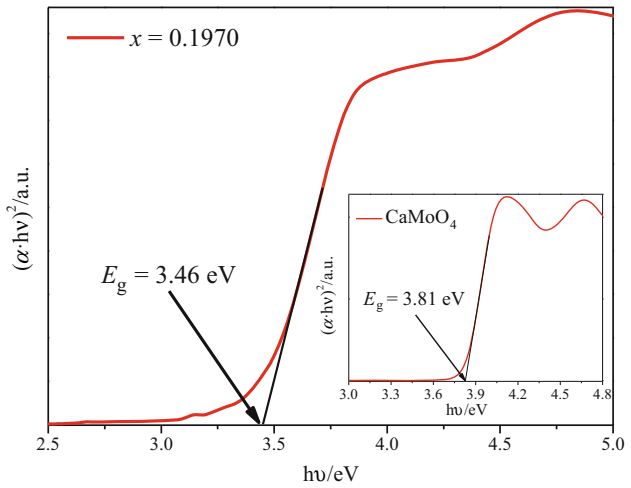

Fig. 12 Plots of $(\alpha \cdot h\nu)^2$ versus $h\nu$ of $CaMoO_4$ (inset) and $Ca_{1-3x-y}Mn_y\square_xEu_{2x}(MoO_4)_{1-3x}(WO_4)_{3x}$ ($x = 0.1970$; $y = 0.0200$) and determined band gap energy

Figure 14 presents an arrangement of chosen EPR spectra detected at *c.a.* 80 K for samples with various manganese ion doping represented by *y* parameter, but with constant europium ion concentration $x = 0.1667$.

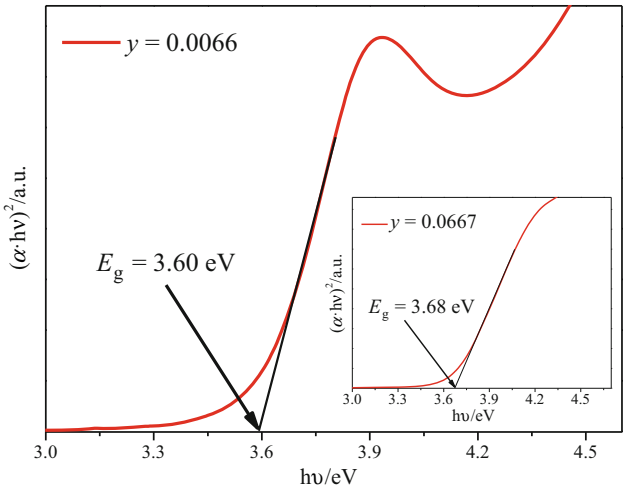

Fig. 13 Plots of $(\alpha \cdot h\nu)^2$ versus $h\nu$ of $Ca_{1-3x-y}Mn_y\square_xEu_{2x}(MoO_4)_{1-3x}(WO_4)_{3x}$ ($y = 0.0667$; x = 0.1667 (inset) and $y = 0.0066$; $x = 0.1667$) and determined band gap energy

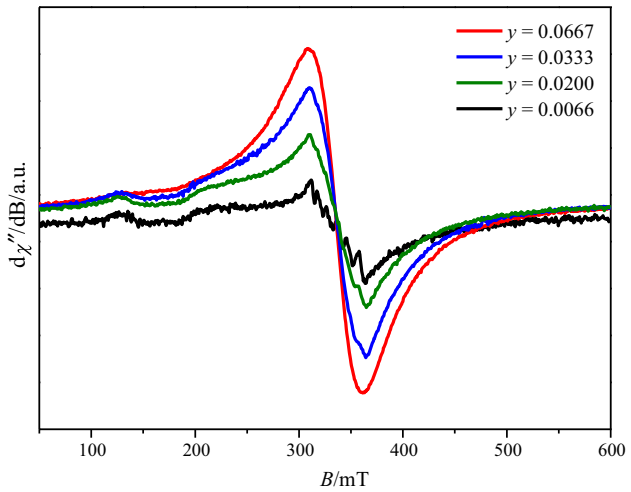

Fig. 14 EPR spectra of Mn^{2+} ions detected at different manganese content represented by *y* parameter

As could be seen in Fig. 14, for samples with lower Mn^{2+} doping the obtained EPR signal possesses six quite well-resolved lines originated from hyperfine interactions between electronic and nuclear magnetic moment of Mn^{2+} ions. But such model works properly only for low-density Mn^{2+} ions. With increasing manganese content, the arrangement of Mn^{2+} ions starts to be systematically disturbed, finally giving only single wide resonance line for samples with *y* parameter above 0.0200.

Figure 15 shows the evolution of EPR spectra under europium doping variation, represented by *x* parameter, while manganese ion concentration is maintained at constant value $y = 0.0200$. As could be seen, relatively low Eu^{3+} concentration gives no influence on the manganese ions. Thus, a well-resolved hyperfine structure of six

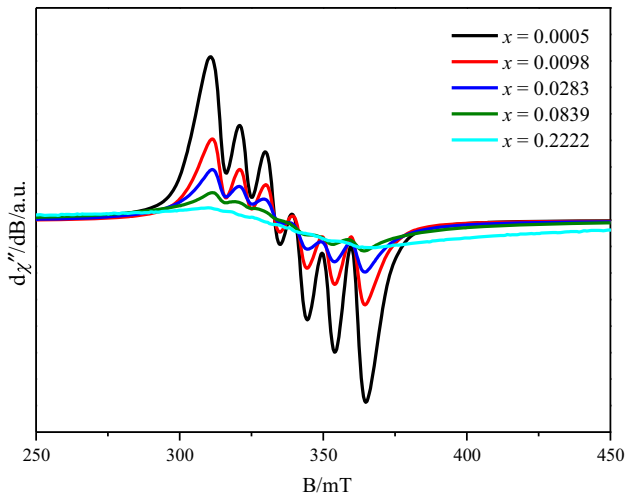

Fig. 15 EPR spectra of Mn^{2+} ions detected at different europium content represented by x parameter

narrow lines is observed. Increase in europium doping leads to situation, where resonance signal is systematically overleaped. For x value 0.2222 and higher, the sixfold arrangement is invisible and the manganese signal consists of only one wide line.

Influence of y parameters on the EPR signal seems to be very expectable. If concentration of manganese is maintained below some critical value, magnetic system of Mn^{2+} ions could be described with model of isolated magnetic ions with Zeeman interaction, disturbed only by hyperfine interaction of Mn^{2+} nuclear spin. Increasing concentration of manganese leads to perturbation of the simple magnetic model. Additional interactions, mainly exchange and dipolar nature, result in widening and overleaping the overall resonance signal.

Coexistence of Eu^{3+} ions apparently gives no influence on the magnetic system of Mn^{2+}, as trivalent europium is non-magnetic. But results shown in Fig. 15 indicate progressive disturbance of manganese system by the increase in europium ion concentration. Due to comparable ionic size, doped Eu^{3+} ions are incorporated into the Mn^{2+} positions. It leads to generation of charge unequilibrium areas (vacancies) localized near such manganese position. Obviously, number of vacancies directly depends on the level of Eu^{3+} concentration, and it increases with increasing x parameter. Thus, vacancy states are denoted in the proposed formula as $\square_x$.

With higher number of vacancies, their localization near Eu^{3+} ions becomes less restrict. Due to charge compensation effect, vacancies could appear in other places, also near existed Mn^{2+} ions. Interaction between vacancies and manganese disturbs the Mn^{2+} electronic structure. Thus, with increasing x parameter, the EPR signal of Mn^{2+} ions starts to overleap, as is visible in Fig. 15.

Temperature dependence of the EPR signal intensity usually allows to describe the nature of interactions between responsible magnetic particles. All studied samples revealed decrease in the signal intensity (I_{EPR}) with increasing temperature according to the Curie–Weiss law:

$$I_{EPR} = C/(T - \theta), \tag{2}$$

where C is the parameter connected with concentration of magnetic ions and θ is the parameter describing the sign of magnetic interactions.

According to Eq. 2, magnetic arrangement created by manganese ions revealed a strong antiferromagnetic (AFM) interaction proved by significant negative value of θ parameter for all samples. Generally, with increasing concentration of Mn^{2+} or Eu^{3+} the strength of AFM interaction increases, too. Figure 16a shows temperature dependence of the resonance signal and adequate fitting done using Eq. 2 for sample: $Ca_{1-3x-y}Mn_y\square_xEu_{2x}(MoO_4)_{1-3x}(WO_4)_{3x}$with x = 0.0283 and y = 0.0200. The sign of magnetic interactions could be also concluded from drawing of $I_{EPR}.T$ product as a function of temperature (Fig. 16b). Positive loops of calculated values indicate negative value of θ parameter, i.e., domination of AFM interactions among responsible Mn^{2+} ions.

As we mentioned earlier, magnetic properties of manganese ions could be described by Zeeman and hyperfine interactions. Enriched spin-Hamiltonian, including additional interactions with crystal field (fine interactions), should has the following form:

$$H_s = \mu_B BgS + SDS + IAI + \sum B_q^k O_q^k, \tag{3}$$

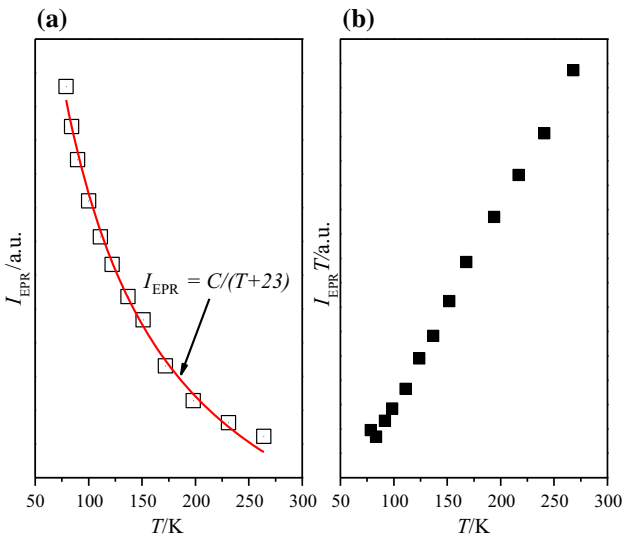

Fig. 16 **a** Intensity of the EPR signal as a function of temperature for sample x = 0.0283, y = 0.0200 (points) and fitting the result using Eq. 1 (line). **b** Dependence of I_{EPR} T product as a function of temperature for sample x = 0.0005 and y = 0.0200

where the first term represents the Zeeman interaction, the second zero-field splitting, the third hyperfine interaction and the last one higher-order fine interactions represented by Stevens operators.

In the case of axial or rhombic symmetry near magnetic particle, the zero-field splitting term could be expressed by standardized form using scalar D value and E parameter represented rhombic distortion near responsible magnetic ions. Thus, useful form of spin-Hamiltonian describing Mn^{2+} ions has the form:

$$H_s = \mu_B BgS + D\left[S_z^2 - \frac{1}{3}S(S+1)\right] + E(S_x^2 - S_y^2) + AIA + \sum B_q^k O_q^k. \quad (4)$$

Equation 4 is employed to simulate the EPR spectra in order to establish: g, D, E, A and B_q^k values. Simulation was done using EPR–NMR program [57]. As we already mentioned, the proposed model seems to be proper only for lower x and y values. Figure 17 presents the best comparison between experimental and simulated spectra using Eq. 4 for sample $x = 0.0098$, $y = 0.0200$. As could be seen, adjustment is quite good. Spin-Hamiltonian values calculated for this case are given in Table 2. Other B_q^k parameters are negligible, $E = 0$. The proposed model is not perfect, but values g_i and A_i are typical for Mn^{2+} ions. From the other hand, zero-field splitting parameter with $D_x = D_y$ indicates an axial symmetry near manganese ions crystallographic positions.

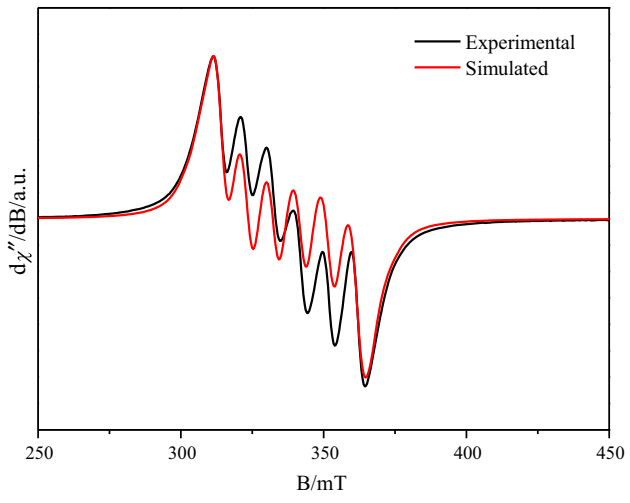

Fig. 17 EPR spectrum of $Ca_{1-3x-y}Mn_y\square_xEu_{2x}(MoO_4)_{1-3x}(WO_4)_{3x}$ with $x = 0.0098$, $y = 0.0200$ (black line) and spectrum simulated using Eq. 3 (red line)

Table 2 Spin-Hamiltonian values calculated by EPR-NMR program for model represented by Eq. 3

	(mT)	(mT)	(mT)
$g_x = 1.998$	$D_x = 0.7$	$A_x = 9.4$	$B_0^4 = 0.03$
$g_y = 2.000$	$D_y = 0.7$	$A_y = 9.4$	$B_{-2}^4 = 0.07$
$g_z = 2.002$	$D_z = -1.4$	$A_z = 9.4$	$B_{-4}^4 = 0.12$

Conclusions

In summary, samples of new Mn^{2+}-doped and Eu^{3+}-co-doped calcium molybdato-tungstates with the formula of $Ca_{1-3x-y}Mn_y\square_xEu_{2x}(MoO_4)_{1-3x}(WO_4)_{3x}$, where $\square$ represents vacancy with different Mn^{2+} (y = 0.0066; 0.0200; 0.0333; 0.0667) as well as Eu^{3+} (x = 0.0005; 0.0025; 0.0050; 0.0098; 0.0283; 0.0455; 0.0839; 0.1430; 0.1667; 0.1970; 0.2059; 0.2222) contents, were successfully obtained by a high-temperature sintering. The XRD patterns showed that doped materials have tetragonal, body-centered scheelite-type structure with space group $I4_1/a$. The melting point of each Mn^{2+}-doped and Eu^{3+}-co-doped material is lower than the melting of pure matrix ($CaMoO_4$, 1753 K), and it strongly depends on Mn^{2+} as well as Eu^{3+} contents in scheelite-type framework. IR results confirmed the presence of MoO_4 and WO_4 tetrahedra, the deformation of their shape in comparison with the tetrahedral shape of regular MoO_4 and WO_4 polyhedra as well as very weak covalent nature of Mo–O and W–O bonds in doped materials. The Tauc plots were used to extrapolate a direct band gap of new ceramics. They are insulators with the optical direct band gap higher than 3.50 eV. For all doped ceramics, E_g values are lower than the direct band gap of pure matrix and they change non-linearly with increasing Mn^{2+} and Eu^{3+} contents. EPR spectra confirmed the existence of magnetic species in the form of Mn^{2+} ions. Manganese ions behave as isolated magnetic centers, if concentration of Mn^{2+} is low. These ions are characterized by close to axial local symmetry, with significant AFM interactions among each other. Increasing manganese ions concentration leads to significant changes in a simple magnetic arrangement, where above y = 0.0200 a complex magnetic system of manganese is created. From the other hand, magnetic arrangement should be also changed by increasing concentration of europium ions. In this case, Eu^{3+} ions have influence on magnetic system by indirect interactions with Mn^{2+} ions. Model with isolated manganese species is changed at europium concentration above $x = 0.2222$.

References

1. Sleight AW. Accurate cell dimensions for ABO_4 molybdates and tungstates. Acta Crystallogr. 1972;B28:2899–902.
2. Santamaria-Perez D, Errandonea D, Rodriguez-Hernandez P, Munoz A, Lacomba-Perales R, Polian A, Meng Y. Polymorphism in strontium tungstate $SrWO_4$ under quasi-hydrostatic compression. Inorg Chem. 2016;55:10406–14.
3. Cavalcante LS, Longo VM, Sczancoski JC, Alemeida MAP, Batista AA, Varela JA, Orlandi MO, Longo E, Siu Li M. Electronic structure, growth mechanism and photoluminescence of $CaWO_4$ crystals. CrystEngComm. 2012;14:853–68.
4. Macavei J, Schulz H. The crystal structure of wolframite type tungstates at high pressure. Z Krystall. 1993;207:193–208.
5. Christofilo D, Ves S, Kourouklis GA. Pressure induced phase transitions in alkaline earth tungstates. Phys Status Solidi B. 1996;198:539–44.
6. Daturi M, Busca G, Borel MM, Leclaire A, Piaggio P. Vibrational and XRD study of the system $CdWO_4$–$CdMoO_4$. J Phys Chem B. 1997;101:4358–69.
7. Manjon FJ, Errandonea D, Garro N, Pellicer-Porres J, López-Solano J, Rodríguez-Hernández P, Radescu S, Mujica A, Muñoz A. Lattice dynamics study of scheelite tungstates under high pressure II. $PbWO_4$. Phys Rev B. 2006;74:112–44.
8. Ronda CR, Jüstel T, Nikol H. Rare earth phosphors: fundamentals and applications. J Alloys Compd. 1998;277(275):669–76.
9. Czajka J, Piskuła Z, Szczeszak A, Lis S. Structural, morphology and luminescence properties of mixed calcium molybdate-tungstate microcrystals doped with Eu^{3+} ions and changes of the color emission chromaticity. Opt Mater. 2018;84:426–33.
10. Cao R, Wang W, Zhang J, Ye Y, Chen T, Guo S, Xiao F, Luo Z. Luminescence properties of $Sr_2Mg_3P_4O_{15}$:Mn^{2+} phosphor and the improvement by co-doping Bi^{3+}. Opt Mater. 2018;79:223–6.
11. Kubus M, Castro C, Enseling D, Jüstel T. Room temperature red emitting carbodiimide compound $Ca(CN_2)$:Mn^{2+}. Opt Mater. 2016;59:126–9.
12. Han B, Li P, Zhang J, Jin L, Luo W, Shi H. β-Zn_3BPO_7:Mn^{2+}: a novel rare-earth-free possible deep-red emitting phosphor. Opt Mater. 2015;42:476–8.
13. Cao R, Shi Z, Quan G, Hu Z, Zheng G, Chen T, Guo S, Ao H. Rare-earth free broadband $Ca_3Mg_3P_4O_{16}$:Mn^{2+} red phosphor: synthesis and luminescence properties. J Lumin. 2018;194:542–6.
14. Chen C, Cai P, Qin L, Wang J, Bi S, Huang Y, Seo HJ. Luminescence properties of sodalite-type $Zn_4B_6O_{13}$:Mn^{2+}. J Lumin. 2018;199:154–9.
15. Song E, Zhao W, Dou X, Zhu Y, Yi S, Min H. Nonradiative energy transfer from Mn^{2+} to Eu^{3+} in $K_2CaP_2O_7$:Mn^{2+}, Eu^{3+} phosphor. J Lumin. 2012;132:1462–7.
16. Katayama Y, Kayumi T, Ueda J, Tanabe S. Enhanced persistent red luminescence in Mn^{2+}-doped (Mg, Zn)GeO_3 by electron trap and conduction band engineering. Opt Mater. 2018;79:147–51.
17. Tomaszewicz E, Filipek E, Fuks H, Typek J. Thermal and magnetic properties of new scheelite type $Cd_{1-3x}\square_xGd_{2x}MoO_4$ ceramic materials. J Eur Ceram Soc. 2014;34:1511–22.
18. Tomaszewicz E, Dąbrowska G, Filipek E, Fuks H, Typek J. New scheelite-type $Cd_{1-3x}\square_xRE_{2x}(MoO_4)_{1-3x}(WO_4)_{3x}$ ceramics—their structure, thermal and magnetic properties. Ceram Int. 2016;42:6673–81.
19. Guzik M, Tomaszewicz E, Guyot Y, Legendziewicz J, Boulon G. Eu^{3+} luminescence from different sites in scheelite-type cadmium molybdate red phosphor with vacancies. J Mater Chem C. 2015;3:8582–94.
20. Guzik M, Tomaszewicz E, Guyot Y, Legendziewicz J, Boulon G. Structural and spectroscopic characterizations of new vacancied $Cd_{1-3x}Nd_{2x}\square_xMoO_4$ scheelite-type molybdates as potential optical materials. J Mater Chem C. 2015;3:4057–69.
21. Guzik M, Tomaszewicz E, Guyot Y, Legendziewicz J, Boulon G. Spectroscopic properties, concentration quenching and Yb^{3+} site occupations in a vacancied scheelite-type molybdates. J Lumin. 2016;169:755–64.
22. Tomaszewicz E, Piątkowska M, Pawlikowska M, Groń T, Oboz M, Sawicki B, Urbanowicz P. New vacancied and Dy^{3+}-doped molybdates—their structure, thermal stability, electrical and magnetic properties. Ceram Int. 2016;42(16):18357–67.
23. Piątkowska M, Tomaszewicz E. Synthesis, structure and thermal stability of new scheelite-type $Pb_{1-3x}\square_xPr_{2x}(MoO_4)_{1-3x}(WO_4)_{3x}$ ceramic materials. J Therm Anal Calorim. 2016;126(1):111–9.
24. Piątkowska M, Tomaszewicz E. Solid-state synthesis, thermal stability and optical properties of new scheelite-type $Pb_{1-3x}\square_xPr_{2x}WO_4$ ceramics. Mater Lett. 2016;182:332–5.
25. Piątkowska M, Fuks H, Tomaszewicz E, Kochmańska AE. New vacancied and Gd^{3+}-doped lead molybdato-tungstates and tungstates prepared via solid state and citrate-nitrate combustion method. Ceram Int. 2017;43(10):7839–50.
26. Pawlikowska M, Piątkowska M, Tomaszewicz E. Synthesis and thermal stability of rare-earths molybdates and tungstates with fluorite and scheelite-type structure. J Therm Anal Calorim. 2017;130(1):69–76.
27. Keskar M, Krishnan K, Phatak R, Dash S, Sali SK, Kannan S. Studies on thermophysical properties of the ThW_2O_8 and UWO_6. J Therm Anal Calorim. 2016;126(2):659–70.
28. Yanase I, Ootomo R, Kobayashi H. Effect of B substitution on thermal changes of UV–Vis and Raman spectra and color of $Al_2W_3O_{12}$ powder. J Therm Anal Calorim. 2018;132:1–6.
29. Łącz A, Bak B, Lach R. Structure, microstructure and physicochemical properties of $BaW_{1-x}Nb_xO_{4-\delta}$ materials. J Therm Anal Calorim. 2018;133(1):107–14.
30. Tabero P, Frąckowiak A. Reinvestigations of the Li_2O–WO_3 system. J Therm Anal Calorim. 2017;130(1):311–8.
31. Tabero P, Frąckowiak A. Synthesis of $Fe_8V_{10}W_{16}O_{85}$ by a solution method. J Therm Anal Calorim. 2016;125(3):1445–51.
32. Pawlikowska M, Fuks H, Tomaszewicz E. Solid state and combustion synthesis of Mn^{2+}-doped scheelites—their optical and magnetic properties. Ceram Int. 2017;43(16):14135–45.
33. Shannon RD. Revised effective ionic radii and systematic studies of interatomic distances in halides and chalcogenides. Acta Crystallogr A. 1976;32:751–67.
34. Clearfield A, Moini A, Rudolf PR. Preparation and structure of manganese molybdates. Inorg Chem. 1985;24:4606–9.
35. Tomaszewicz E, Fuks H, Typek J, Sawicki B, Oboz M, Groń T, Mydlarz T. Preparation, thermal stability and magnetic properties of new $AgY_{1-x}Gd_x(WO_4)_2$ ceramic materials. Ceram Int. 2015;41(4):5734–48.
36. Liegeois-Duyckaerts M, Tarte P. Vibrational studies of molybdates, tungstates and related compounds—II: new Raman data and assignments for the scheelite-type compounds. Spectrochim Acta A. 1972;28(11):2037–51.
37. Brown RG, Denning J, Hallett A, Ross SD. Forbidden transitions in the infra-red spectra of tetrahedral anions—VIII: spectra and structures of molybdates, tungstates and periodates of the formula MXO_4. Spectrochim Acta A. 1970;26(4):963–70.
38. Tarte P, Liegeois-Duyckaerts M. Vibrational studies of molybdates, tungstates and related compounds—I: new infrared data

and assignments for the scheelite-type compounds $X^{II}MoO_4$ and $X^{II}WO_4$. Spectrochim Acta A. 1972;28(11):2029–36.
39. Khanna RK, Lippincott ER. Infrared spectra of some scheelite structures. Spectrochim Acta A. 1968;24:905–8.
40. Hanuza J, Macalik L. Polarized i.r. and Raman spectra of orthorhombic $KLn(MoO_4)_2$ crystals (Ln = Y, Dy, Ho, Er, Tm, Yb, Lu). Spectrochim Acta. 1982;38(1):61–72.
41. Hanuza J, Mączka M, van der Maas JH. Polarized IR and Raman spectra of tetragonal $NaBi(WO_4)_2$, $NaBi(MoO_4)_2$ and $LiBi(MoO_4)_2$ single crystals with scheelite structure. J Mol Struct. 1995;348:349–52.
42. Godlewska P, Tomaszewicz E, Macalik L, Hanuza J, Ptak M, Tomaszewski PE, Ropuszyńska-Robak P. Structure and vibrational properties of scheelite type $Cd_{0.25}RE_{0.5}\square_{0.25}MoO_4$ solid solutions where □ is the cationic vacancy and RE = Sm–Dy. J Mol Struct. 2013;1037:332–7.
43. Godlewska P, Tomaszewicz E, Macalik L, Hanuza J, Ptak M, Tomaszewski PE, Mączka M, Ropuszyńksa-Robak P. Correlation between the structural and spectroscopic parameters for $Cd_{1-3x}Gd_{2x}\square_xMoO_4$ solid solutions where □ denotes cationic vacancies. Mater Chem Phys. 2013;139(2–3):890–6.
44. Kubelka P, Munk F. Ein Beitrag zur Optic der Farbanstriche. Z Tech Phys. 1931;12:593–601.
45. Urbanowicz P, Piątkowska M, Sawicki B, Groń T, Kukuła Z, Tomaszewicz E. Dielectric properties of $RE_2W_2O_9$ (RE = Pr, Sm–Gd) ceramics. J Eur Ceram Soc. 2015;35(15):4189–93.
46. Franco A Jr, Pessoni HV. Optical band-gap and dielectric behavior in Ho—doped ZnO nanoparticles. Mater Lett. 2016;180:305–8.
47. Hone FG, Ampong FK, Abza T, Nkrumah I, Paal M, Nkum RK, Boakye F. The effect of deposition time on the structural, morphological and optical band gap of lead selenide thin films synthesized by chemical bath deposition method. Mater Lett. 2015;155:58–61.
48. Si S, Deng H, Zhou W, Wang T, Yang P, Chu J. Modified structure and optical band-gap in perovskite ferroelectric $(1-x)KNbO_3$–$xBaCo_{1/3}Nb_{2/3}O_3$ ceramics. Ceram Int. 2018;44(12):14638–44.
49. Lee HJ, Lee JA, Lee JH, Heo YW, Kim JJ, Park SK, Limb J. Optical band gap modulation by Mg-doping in $In_2O_3(ZnO)_3$ ceramics. Ceram Int. 2012;38:6693–7.
50. Tauc J, Grigorovici R, Vancu A. Optical properties and electronic structures of amorphous germanium. Phys Status Solidi. 1996;15:627–37.
51. Tauc J, Menth A. States in the gap. J Non-Cryst Solids. 1972;8–10:569–85.
52. Lacomba-Perales R, Ruiz-Fuertes J, Errandonea D, Martinez-Garcia D, Segura A. Optical absorption of divalent metal tungstates: correlation between the band-gap energy and the cation ionic radius. EPL. 2008;83:37002.
53. Pontes FM, Maurera MAMA, Souza AG, Longo E, Leite ER, Magnani R, Machado MAC, Pizani PS, Varela JA. Preparation, structural and optical characterization of $BaWO_4$ and $PbWO_4$ thin films prepared by a chemical route. J Eur Ceram Soc. 2003;23(16):3001–7.
54. Zhang Y, Holzwarth NAW, Williams RT. Electronic band structure of the scheelite materials $CaMoO_4$, $CaWO_4$, $PbMoO_4$, and $PbWO_4$. Phys Rev B. 1998;57(20):12738–50.
55. Maurera MAMA, Souza AG, Soledade LAB, Pontes FM, Longo E, Leite ER, Varela JA. Microstructural and optical characterization of $CaWO_4$ and $SrWO_4$ thin films prepared by a chemical solution method. Mater Lett. 2004;58(5):727–32.
56. Singh BP, Parchur AK, Ningthoujam RS, Ansan AA, Singh P, Rai SB. Enhanced photoluminescence in $CaMoO_4$: Eu^{3+} by Gd^{3+} co-doping. Dalton Trans. 2014;43:4779–89.
57. Mombourquette MJ, Weil JA, McGavin DG. EPR–NMR user's manual. Saskatoon: Department of Chemistry University of Saskatchewan Saskatoon; 1999.